# Strain Partitioning in the Southeastern Tibetan Plateau From Kinematic Modeling of High-Resolution Sentinel-1 InSAR and GNSS

Jin Fang[1] , Tim J. Wright[1] , Kaj M. Johnson[2] , Qi Ou[1,3] , Richard Styron[4] , Tim J. Craig[1] , John R. Elliott[1] , Andy Hooper[1] , and Gang Zheng[1]

[1]COMET, School of Earth and Environment, University of Leeds, Leeds, UK, [2]Department of Earth and Atmospheric Sciences, Indiana University, Bloomington, IN, USA, [3]Now at COMET, Global Change Institute, School of GeoSciences, University of Edinburgh, Edinburgh, UK, [4]Global Earthquake Model Foundation, Pavia, Italy

**Abstract** Fault slip rates estimated from geodetic data are being integrated into seismic hazard models. The standard approach requires modeling velocities and relative (micro-)plate motions, which is challenging for fault-based models. We present a new approach to directly invert strain rates to solve for slip rates and distributed strain simultaneously. We generate velocity and strain rate fields over the southeastern Tibetan Plateau, utilizing Sentinel-1 Interferometric Synthetic Aperture Radar data spanning 2014–2023. We derive slip rates using block modeling and by inverting strain rates. Our results show a partitioning between localized strain on faults and distributed deformation. The direct inversion of strain rates matches the geodetic data best when incorporating distributed moment sources, accounting for a similar proportion to on-fault sources. The direct strain methodology also aligns best with the independent geological slip rates, especially near fault tips. As high-resolution strain rate fields become increasingly available, we recommend direct inversion as the preferred practice.

**Plain Language Summary** We focus on understanding earthquake potential in the southeastern Tibetan Plateau by measuring how and how fast the crust deforms. By analyzing 9 years of satellite radar images, we estimate how fast faults are slipping, which is crucial for assessing the hazard of future earthquakes. We tested two methods and found that the method directly incorporating measurements of surface strain rates provides more accurate results when compared to field-based geologic slip rates. We show that the total deformation field is roughly equally split between energy accumulation on mapped active faults and distributed deformation away from the faults. The large amount of diffuse strain is an important constraint for rates of background seismicity. We discuss the limitations of various techniques used in modeling Earth's interseismic deformation and suggest prioritizing the direct strain methodology.

## 1. Introduction

Fault slip rates are a fundamental component for seismic hazard analyses. However, the Tibetan Plateau lacks comprehensive geological sources for slip rates on numerous faults, with very few field-based slip rate estimates (Styron, 2022, and references therein), compared to the geological deformation models in the Western United States (Hatem et al., 2022) and New Zealand (Van Dissen et al., 2023).

Satellite geodetic data, such as Global Navigation Satellite System (GNSS) and Interferometric Synthetic Aperture Radar (InSAR), are regularly used to determine fault slip rates. A growing number of geodetic modeling approaches are being applied, including elastic block models (Evans, 2022; Hammond et al., 2024; McCaffrey, 2009; Meade & Loveless, 2009; Shen et al., 2015; Styron, 2022), deep dislocation models (Elston et al., 2024; Zeng, 2022; Zeng & Shen, 2014, 2017), NeoKinema—a kinematic finite element approach to estimate fault slip rates and off-fault strains (Bird, 2009; Shen & Bird, 2022), viscoelastic fault models (Pollitz, 2022; Pollitz et al., 2010; Pollitz & Evans, 2017), and viscoelastic earthquake cycle block models (Chuang & Johnson, 2011; DeVries et al., 2017; Johnson & Fukuda, 2010; Pollitz & Evans, 2017). Among these techniques, geodetically-derived surface velocity data are used as the primary constraints in models, alongside geologically-derived slip rates typically applied as a prior constraint. In contrast, a recently developed method by Johnson et al. (2024) inverts geodetic strain rates directly for slip deficit rates (moment accumulation rates) on faults. An advantage of inverting strain rate fields is that rigid block rotations can be ignored, which means that tectonic

blocks (or microplates) do not need to be defined. The assumption in block models and the direct inversion method of Johnson et al. (2024), is that the majority of the surface strain rate field derives from elastic distortion due to slip deficit (coupling) on faults. However, high-resolution (e.g., 1 km or better) strain rate data is required to obtain robust estimates of slip deficit rate and distributed strain.

In this study, we focus on the southeastern Tibetan Plateau, utilizing the Sentinel-1 InSAR data spanning the period between 2014 and 2023, along with the published GNSS velocities (Fang, Houseman, et al., 2024, and references therein), to obtain large-scale high-resolution velocity and strain rate fields. We derive slip or slip deficit rates on recently mapped faults (Styron, 2022) through classic block modeling and "deformable block" modeling (Meade & Loveless, 2009), as well as through the direct inversion of strain rates (Johnson et al., 2024). The data sets and models enable us to investigate and quantify the partitioning of localized and diffuse strain in the region. We review and compare different geodetic approaches to modeling deformation. We observe significant distributed strain and discuss the implications.

## 2. Geodetic Data

We employ the LiCSAR (Lazecky et al., 2020) and LiCSBAS (Morishita et al., 2020) processing chain to obtain average line-of-sight (LOS) velocities at a resolution of ~1 km from Sentinel-1 satellite data (35 ascending and 32 descending frames, Figure 1 and Table S1 in Supporting Information S1). Combining InSAR LOS velocities with published GNSS data (Fang, Houseman, et al., 2024, and references therein), we obtain a unified velocity field in a Eurasia-fixed reference frame following the VELMAP approach (H. Wang & Wright, 2012). Eastward and vertical velocities are subsequently decomposed pixel by pixel directly from the referenced LOS velocities using the interpolated, smoothed north-south component of the GNSS velocities as constraints (Hussain et al., 2018; Ou et al., 2022; Weiss et al., 2020; Wright et al., 2004). We calculate the strain rate fields directly from gradients of Gaussian-filtered (with a sigma of 10 pixels, corresponding to ~10 km) InSAR eastward velocities and interpolated GNSS northward velocities. Further details can be found in Texts S1–S2 in Supporting Information S1.

## 3. Kinematic Modeling

### 3.1. Block Modeling

We use the *Blocks* code (Meade & Loveless, 2009) to estimate block rotations and slip rates on recently updated active faults (Styron, 2022), considering both classic rigid block modeling and "deformable block" modeling, which allows for internal strain. Our model comprises 103 blocks bounded by 326 fault sections in the southeastern Tibetan Plateau, with slip rates and coupling constrained by the combined geodetic velocities at 6,617 observation points from the VELMAP approach (Text S2 in Supporting Information S1). We assume a uniform locking depth of 20 km, where the lowest root-mean-square (RMS) of residual strain rates is observed (Figure S7 in Supporting Information S1). The block model is relatively insensitive to variations within the locking depth range of 15–30 km, consistent with previous studies (Loveless & Meade, 2011; W. Wang et al., 2021; D. Zhao et al., 2024). More details can be found in Text S3 in Supporting Information S1.

### 3.2. Inverting Strain Rates for Slip Deficit Rates

We construct a 3-D fault model, aligning its geometry with that of the block models (Section 3.1 and Text S3 in Supporting Information S1), focusing specifically on the area covered by high-resolution strain rate observations. Structures outside of the coverage are excluded from the model. We fix the rake for model faults to the preferred value based on Shan et al. (2009) and fault kinetic properties documented by Xu (2022) (Figure S9 in Supporting Information S1). The rectangular fault sections extend at a constant dip from the surface to a depth of 20 km, discretized into 3 equal elements along the dip direction. Before inversion, we downsample the strain rate observations using a nested uniform downsampling approach. The region within ~50 km of the model faults is downsampled 100 times (i.e., ~10 km resolution sampling), while beyond this region, a downsampling of 200 times is applied. This results in a total of ~21,000 strain rate measurements (3 strain rate components at ~7,000 observation points), which are used for inversion using the code *SlideFS* (Johnson, 2024; Johnson et al., 2024).

We build on the approach of Johnson et al. (2024) to estimate distributed moment sources in addition to slip deficit rates on faults. The strain rates due to slip deficit on faults are calculated at the centroids of triangles of a fault-based triangular mesh and interpolated to the observation points; the triangular mesh is generated using
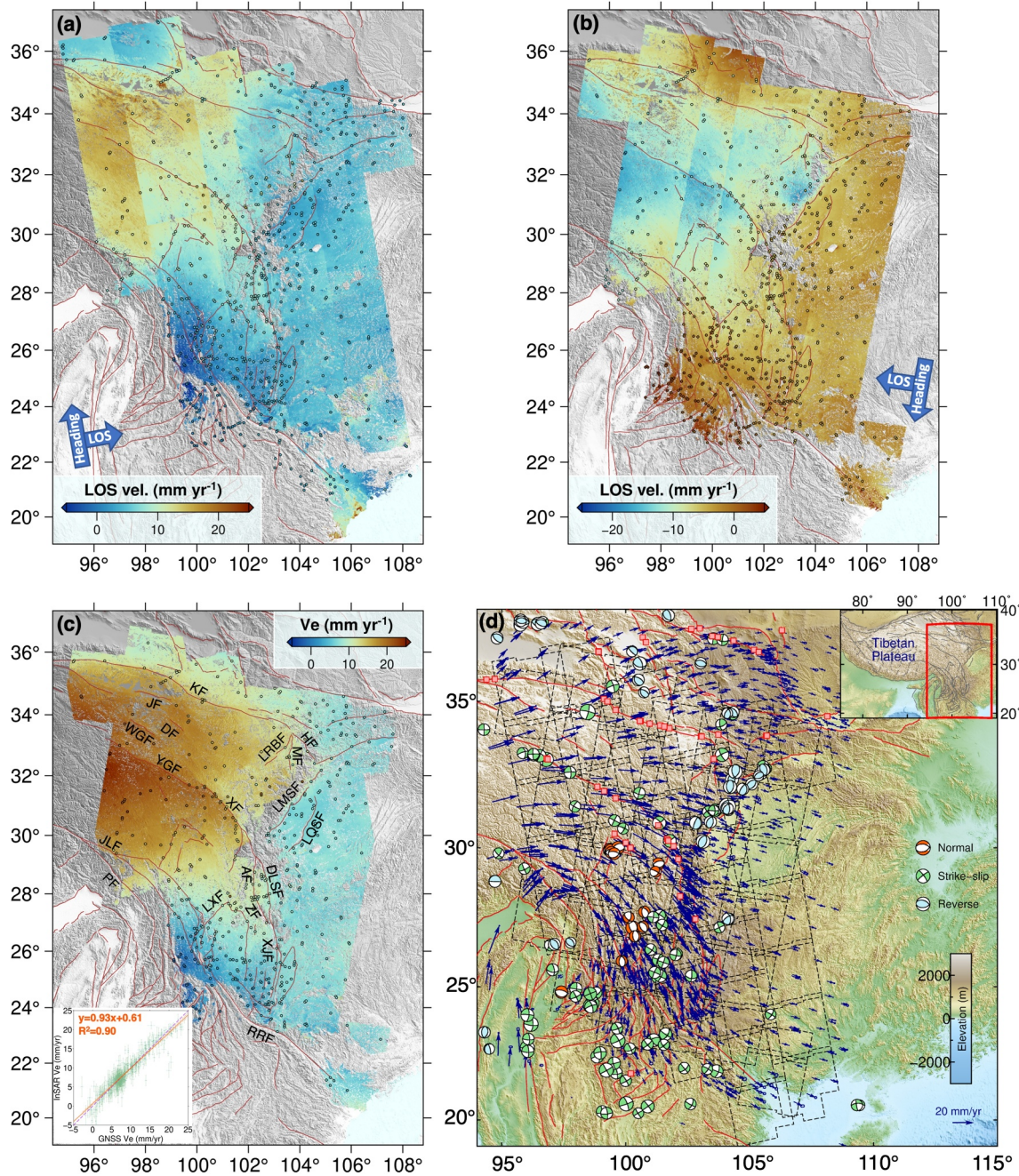
**Figure 1.** (a) Ascending and (b) descending LOS velocity mosaics in a Eurasia-fixed reference frame defined by Global Navigation Satellite System (GNSS). Colored dots are GNSS LOS rates. (c) Interferometric Synthetic Aperture Radar (InSAR) eastward velocity field ($V_E$) at ∼1 km resolution, derived from direct decomposition of (a, b). Colored dots represent GNSS eastward velocities. Inset map in panel (c) shows regression of comparison between InSAR and GNSS $V_E$. Red solid line and purple dashed line denote best-fit linear model and one-to-one line for reference, respectively. AF, Anninghe Fault; DF, Dari Fault; DLSF, Daliangshan Fault; HF, Huya Fault; JF, Jiangcuo Fault; JLF, Jiali Fault; KF, Kunlun Fault; LMSF, Longmenshan Fault; LQSF, Longquanshan Fault; LRBF, Longriba Fault; LXF, Lijiang-Xiaojinhe Fault; MF, Minjiang Fault; PF, Puqu Fault; RRF, Red River Fault; WGF, Wudaoliang-Gongma Fault; XF, Xianshuihe Fault; XJF, Xiaojiang Fault; YGF, Yushu-Ganzi Fault; ZF, Zemuhe Fault. (d) Tectonic setting for study area (red rectangle in the inset). Red lines depict active fault traces from a new fault database updated by Styron (2022). Beach balls show the locations and focal mechanisms of earthquakes from the GCMT catalog (Dziewonski et al., 1981; Ekström et al., 2012). Dashed-line polygons delimit the spatial coverage of Sentinel-1 InSAR data used in this study. GNSS horizontal velocities (Fang, Houseman, et al., 2024, and references therein) are shown as dark blue vectors. Red squares show available geologic fault slip rates (compiled by Styron, 2022).

MESH2D (Engwirda, 2014), with fault segment endpoints as nodes and fault traces as sides of triangles (Figure S10 in Supporting Information S1). We also compute three horizontal moment tensor components at a distribution of nodes forming a uniform triangular mesh with node spacing of roughly 50 km (Figure S11 in Supporting Information S1). We populate a thin elastic plate (plane stress conditions) with force couples located at the nodes of the uniform mesh, compute strain rates at the centroids of the triangles, and interpolate to observation points. The distributed moment sources represent depth-averaged diffuse deformation in the crust and may represent elastic moment accumulation (elastic storage of energy) or inelastic moment release (largely aseismic rock "flow"). A smoothing factor is used to balance the relative weight between accurately fitting the data and ensuring a smooth distribution of slip deficit rates on faults (first derivative smoothing). We also regularize the inversion by minimizing the magnitude of moment tensor components, which is controlled by a damping parameter. We select our preferred model based on the reduced chi-square statistic ($\chi_v^2 \approx 1$), considering the trade-off between residuals and model roughness, as well as interplay between on-fault and distributed moment rates (Figure S12 in Supporting Information S1). The model with $\chi_v^2$ around 1 indicates that the match between observations and predictions is in accord with the error variance ($\chi_v^2 < 1$ overfitting the noise while $\chi_v^2 > 1$ underfitting the data, Figure S13 in Supporting Information S1). Considering geologic slip rates as independent measurements (not used as constraints in the inversion), we impose a loose upper bound of 30 mm/yr on the slip deficit rate of each fault. This bound is further scaled by a factor of 10 to ensure it is applied in a very loose manner. More details about the inversion scheme can be found in Johnson et al. (2024) and Text S4 in Supporting Information S1.

## 4. Results

### 4.1. Velocity and Strain Rate Fields

The Eurasia-fixed ascending and descending LOS velocities provide a detailed map of surface motion in the southeastern Tibetan Plateau (Figure 1). The resulting east-west velocity field shows large-scale eastward motion of the high plateau relative to Eurasia, with a peak rate of 25 mm/yr occurring in the area between the Jiali and Yushu-Xianshuihe faults. Outside the plateau, eastward velocities decrease to 5–10 mm/yr in the east and exhibit westward motion of 5 mm/yr in the southwest. Notably, a prominent characteristic is the apparent velocity contrasts observed across the major faults that represent strain concentrations on these structures (Figure 2), including the Kunlun, Yushu-Xianshuihe-Xiaojiang, Longriba, Longmenshan, and Lijiang-Xiaojinhe faults. The Xianshuihe fault shows the sharpest velocity transition where shallow creep has been previously identified (Li & Bürgmann, 2021; Qiao & Zhou, 2021). The velocity difference across the Longmenshan Fault is likely influenced by the ongoing postseismic deformation of the 2008 $M_W$ 7.9 Wenchuan earthquake (e.g., M. Wang et al., 2021). Our combined geodetic horizontal velocities derived from the VELMAP approach fit the GNSS observations with an RMS of 1.3 mm/yr and match the InSAR measurements with an RMS of 0.6 mm/yr. The ascending and descending LOS velocities agree with GNSS LOS velocities (Figures 1a and 1b), with correlations of 0.74 and 0.75 and slopes of 1.05 and 0.85. The correlation between InSAR and GNSS east velocities ($V_E$) has a slope of 0.93 and an $R^2$ value of 0.90 (Figure 1c).

The high-resolution (∼1 km) InSAR data sharpens the distribution of strain rates along the major faults (Figure 2), compared to GNSS-based strain rate fields typically characterized by a wider distribution of shear strain (Li et al., 2019; Pang et al., 2023; M. Wang & Shen, 2020; G. Zhao et al., 2022; Zhu et al., 2023). Our strain rate fields reveal a partitioning through focused shear on the Kunlun (50–80 nanostrain/year), Yushu-Xianshuihe-Xiaojiang (50–100 nanostrain/year), Longriba (25–50 nanostrain/year), and Lijiang-Xiaojinhe (25–60 nanostrain/year) faults, as well as the Longmenshan fault (50–70 nanostrain/year). The latter is possibly influenced by the ongoing postseismic deformation of the 2008 $M_W$ 7.9 Wenchuan earthquake. On the high plateau (red dashed polygon in Figure 2c,i) there is diffuse deformation away from the major faults, with average shear strain and dilatation rates of 16 and 25 nanostrain/year, compared to 8 and 5 nanostrain/year in the Sichuan basin (which likely reflects the noise floor in the data, purple dotted polygon in Figure 2c,i). Notably, the maximum shear strain rate field shows highly localized strain along the creeping segment of the Xianshuihe fault straining at a rate of ∼100 nanostrain/year. We note that this is a significant underestimate due to our Gaussian filtering applied to the eastward velocity field; the GNSS-derived result gives a lower rate of 40–60 nanostrain/year (e.g., M. Wang & Shen, 2020). The Longmenshan, Xianshuihe, and Jiali faults exhibit contraction rates of ∼50–100 nanostrain/year. However, given the dominance of high-resolution InSAR eastward velocities over interpolated GNSS northward velocities in
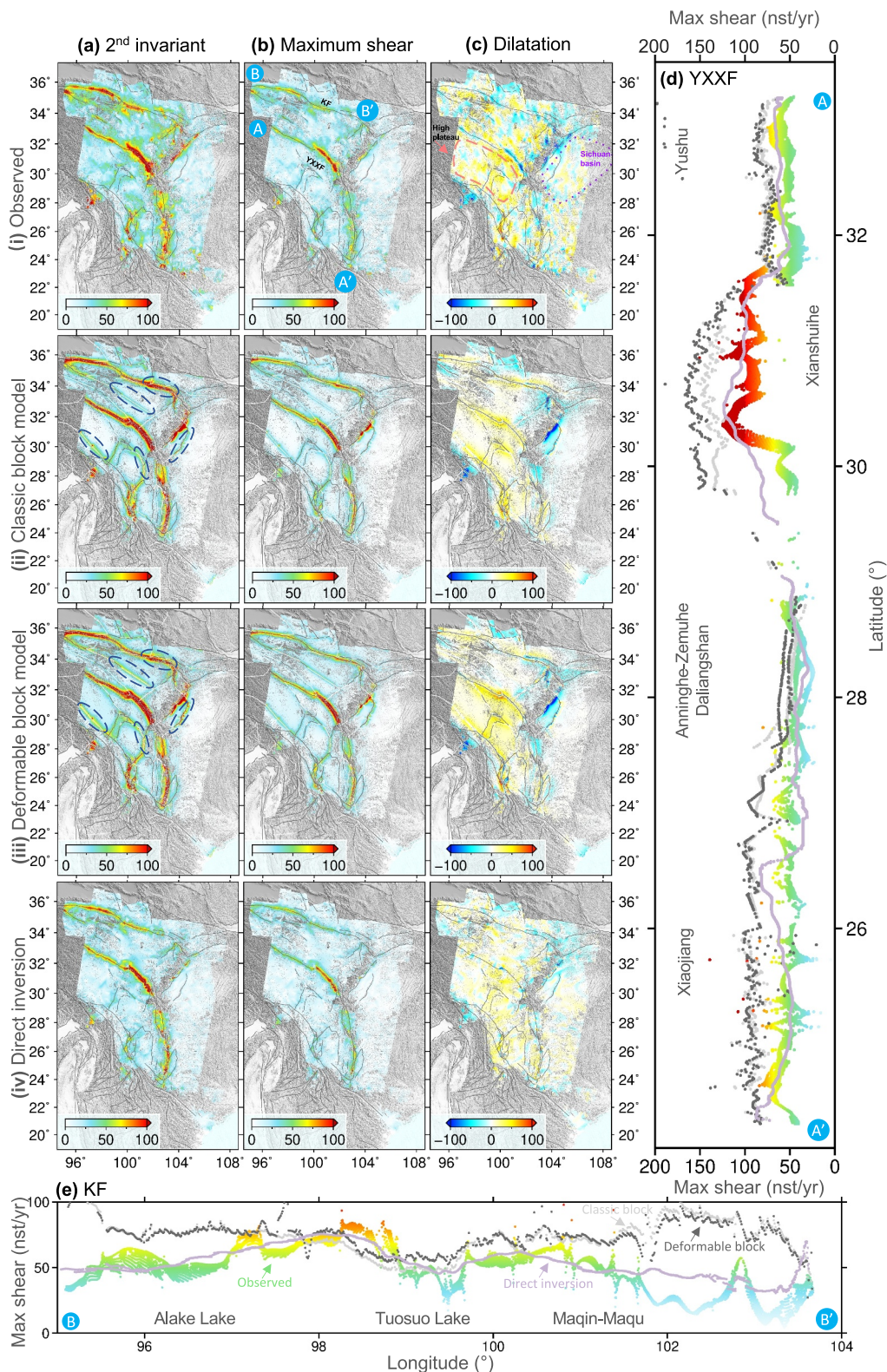
**Figure 2.** (a–c) Comparison of observed and modeled strain rates at the same resolution (∼1 km) using different modeling approaches (left-hand side label). In subplots of block models, non-fault boundaries are shown as white lines. (d–e) Observed and modeled maximum shear strain rates along the Yushu-Xianshuihe-Xiaojiang fault (d) and the Kunlun fault (e). Colored dots represent observations within a 5 km bin. Light gray and dark gray dots denote classic and deformable block models, respectively. Light purple dots are predictions from the direct inversion of strain rates.

determining strain rates, the observed contractional strain is an artifact, as indicated by a simple forward model of creep (Figure S14 in Supporting Information S1).

Classic and deformable block models explain the velocity observations with an RMS of 1.3 mm/yr and 1.1 mm/yr, respectively (Figure S15 in Supporting Information S1). Nevertheless, they fall short in reproducing the strain rate observations (Figure 2). Without accounting for strain in block interiors, the classic block model predicts around 45% (variance reduction) of the observed geodetic strain. By contrast, the deformable block model considering homogeneous intra-block strain explains $\sim 50\%$ of the total strain. The reduced chi-square $(\chi_v^2)$ values of the block models fitted to strain rates are significantly greater than 1, indicating underfitting of the strain rate data (Figure S7 in Supporting Information S1). Notably, the block model tends to overestimate shear strain on faults (Figures 2d and 2e and Figures S16a–S16b in Supporting Information S1), predicting focused strain along block boundaries even in the absence of observed significant strain concentrations (e.g., blue dashed ellipses in Figures 2a,ii and 2a,iii and Figure S8 in Supporting Information S1). The dilatation rate fields obtained from the block models generally exhibit a consistent alignment with the observed patterns. In the region of the high plateau characterized by distributed deformation away from the faults, the average magnitudes of the modeled dilatation rates are 10 and 14 nanostrain/year, representing a discrepancy of 60% and 44% lower than the corresponding observed value (25 nanostrain/year), respectively (Figures S16a–S16b in Supporting Information S1).

By directly inverting strain rates, we suggest that $\sim 40\%$ of the geodetic strain is attributable to elastic coupling (back slip) on model faults, while an additional $\sim 35\%$ is explained by distributed moment sources (Figures 2 and 3d, Figures S17, and S18 in Supporting Information S1). These contribute to $\sim 75\%$ of the total strain, with an RMS of residuals of 9 nanostrain/year and a reduced chi-square $(\chi_v^2)$ value of ~1. The remaining $\sim 25\%$ likely stems from the noise level in the strain rate data and the relatively less precise gradient of northward velocities obtained through interpolation from GNSS. The along-strike variation of maximum shear strain rates aligns well with the observed strain rate data (Figures 2d and 2e). The dilation rate concurs with the observed pattern while slightly underestimating the magnitude, with an average of 20 nanostrain/year in the high plateau (Figure S16c in Supporting Information S1).

### 4.2. Fault Slip (Deficit) Rates

The block models and the strain rate model handle non-strike-slip components differently. In block models, faults with dips other than 90° do not involve tensile-slip; rather, they have a dip-slip component (Meade & Hager, 2005; Meade & Loveless, 2009). The direct inversion of strain rates does not account for fault opening. Besides, there is a limited availability of geologic extensional rates in the region. Therefore, we focus on comparing strike-slip rates in the text. The slip rates determined geodetically from the two block models generally exhibit alignment with the available geologic rates, with correlation coefficients of 0.67 and 0.72, respectively (Figure 3 and Figure S19 in Supporting Information S1). It is worth noting, however, that these models tend to underestimate slip rates on slow-slipping faults ($<\sim 5$ mm/yr) and conversely, overestimate rates on faults that slip faster than $\sim 5$ mm/yr. Particularly noteworthy is the classic block model's slight under-prediction of strike-slip rates on the creeping segment of the Xianshuihe fault, whereas the deformable block model yields more consistent estimates when compared to geologic rates. There is an additional discrepancy in that the deformable block model predicts a slower slip rate on the Zemuhe fault and a faster rate on the Puqu fault (Figure S19a in Supporting Information S1).

In contrast, the slip deficit rates obtained through the direct inversion of strain rates demonstrate greater consistency with available geologic rates, with a higher correlation coefficient of 0.80 (Figure 3 and Figure S19d in Supporting Information S1). Similarly, the slip deficit rates tend to be on the low end of the geologic rates for faults that slip lower than $\sim 5$ mm/yr, while on the high end for faster-slipping faults ($>\sim 5$ mm/yr). This method shows better alignment with the geologic rates, particularly regarding the along-strike variations observed on the Kunlun and Yushu-Xianshuihe-Xiaojiang faults (Figures 3e and 3f). Notably, the direct inversion approach predicts a reduction in slip rates from the Tuosuo Lake segment of the Kunlun fault towards its eastern tip, while the two block models tend to underestimate slip rates on the Tuosuo Lake segment and overestimate rates on the easternmost section of the Kunlun fault (Figure 3f). This discrepancy between the geodetic and geologic rates has been revealed in previously published block models as well (Meade, 2007; Styron, 2022; W. Wang et al., 2021).
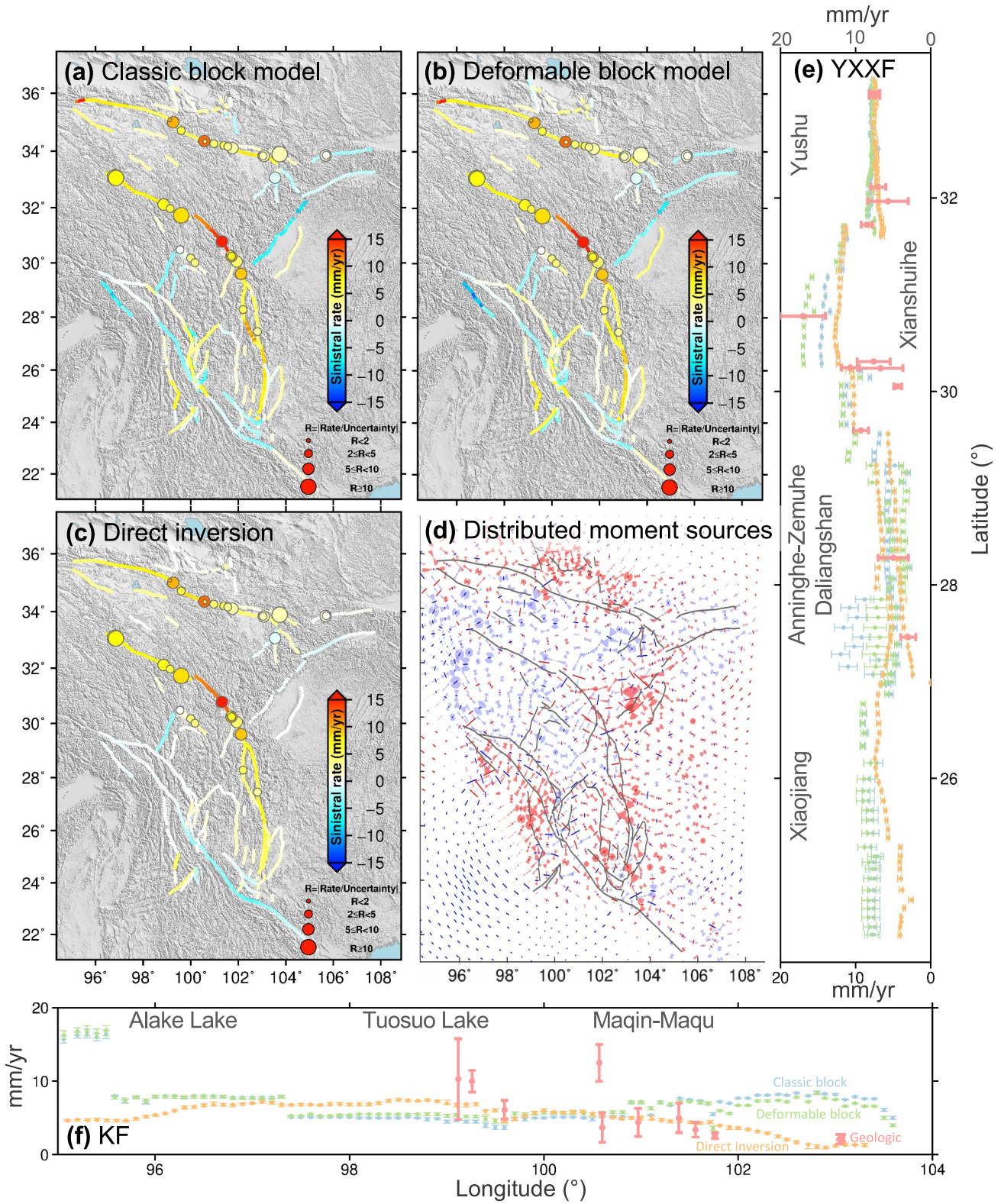
**Figure 3.**

## 5. Discussion

Since the early days of plate tectonics, deformation has been described by the motion of a number of blocks, or microplates (Avouac & Tapponnier, 1993; McKenzie, 1972), although a growing body of evidence has highlighted the limitations of this plate tectonic approximation (e.g., Gordon, 2023). In applying plate tectonics to continental regions, the trend in block models has been to increase the number of blocks to explain more GNSS velocities as they become available (Q. Chen et al., 2004; Li, Shan, et al., 2023; Li, Song, et al., 2023; Loveless & Meade, 2011; Meade, 2007; Shen et al., 2005; Styron, 2022; Thatcher, 2007; W. Wang et al., 2017, 2021). Among all the block models developed for the southeastern Tibetan Plateau, our model is one of the most complete and geologically accurate models based on a recently updated active fault database with a higher resolution (Styron, 2022; D. Zhao et al., 2024). Although the dense block models may be poorly constrained in the southern region with closely-spaced faults, the geodetically-derived rotation rates (Figures S20b and S21b in Supporting Information S1) generally align with paleomagnetic declination anomalies, which are relatively larger toward the south (e.g., Otofuji et al., 2010; Tong et al., 2021). Block models are useful in deriving fault slip rates that generally align with geologic rates, without the need for drawing numerous velocity profiles across faults to fit a screw dislocation model (Li & Bürgmann, 2021; Qiao & Zhou, 2021; Savage & Burford, 1973; Zheng et al., 2017). However, the block models' prediction of strain rates shows inconsistency with the observations, including strain concentrations on block boundaries where no such strain concentration is observed (Figure 2 and Figure S8 in Supporting Information S1); they tend to overestimate shear strains on bounding segments and underestimate diffuse strains in the block interiors (Figures S8 and S16a–S16b in Supporting Information S1). Because faults cannot end in block models, slip rates can only diminish toward the end of large structures if strain is transferred onto other faults.

The deep dislocation model incorporates fault locking by extending faults to infinite depth below a locking depth and then solves for slip rates (Zeng, 2022; Zeng & Shen, 2014, 2017). It requires a few block boundaries to be appended to the fault network; a connectivity constraint is then applied to these boundaries to ensure a smooth variation in along-strike slip rates. Another deep slip model, recently proposed by Elston et al. (2024), recommends the inclusion of interseismic stressing-rate data for enhanced slip rate estimates. Nevertheless, this approach requires the determination of stressing-rate tensors with magnitudes, rather than solely relying on the normalized deviatoric stress tensors provided by focal mechanism inversions. It is worth noting that the stressing-rate does not directly correspond to the absolute stress magnitude (Fialko, 2021).

By contrast, the NeoKinema modeling approach (Bird, 2009; Shen & Bird, 2022) is fault-based, avoiding the need of defining block boundaries and solving for block motions. It uses a triangular finite-element mesh to relate fault slip and distributed off-fault deformation to GNSS velocities and principal stress directions, as well as the geologic slip rates. This method removes elastic locking iteratively using the current model estimates of slip rates and locking depths constrained a priori. This limitation hinders its applicability in regions lacking comprehensive geologic slip rate estimates. Conversely, the viscoelastic fault-based model (Pollitz, 2022; Pollitz et al., 2010; Pollitz & Evans, 2017) solves for distributed moment sources and incorporates time-dependent effect of earthquake cycle deformation due to repeating earthquakes assuming linear viscoelasticity; this assumption does not hold in practice (Hetland & Hager, 2005; Hussain et al., 2018; Lambert & Barbot, 2016). Accounting for time-dependent deformation is likely important as our observed strain rate concentrations on the Longmenshan fault are probably impacted by the postseismic deformation of the 2008 $M_W$ 7.9 Wenchuan earthquake (Figure 2).

In contrast to these geodetic deformation models primarily constrained by velocity data, the direct modeling of strain rates (Johnson et al., 2024) holds a key advantage in immediately determining slip deficit rates (or moment accumulation rates). This method does not require fitting rigid-body rotations that produce zero strain rate. In our

**Figure 3.** (a–c) Comparison of strike-slip rates derived from different modeling methods. (a–b) Estimates from classic and deformable block models. Slip rates on all bounding segments are plotted in Figures S20–S21 in Supporting Information S1. (c) Strike-slip deficit rates converted from the depth-averaged rates via direct inversion of strain rates, using preferred rake values (Figure S9 in Supporting Information S1). Note that we do not remove the creep rates on the Xianshuihe fault from our model. The 3-D distribution of slip deficit rates is shown in Figure S22 in Supporting Information S1. Each colored dot in panels (a–c) represents the best geologic estimate, with the size scaled by the ratio of the rate to its uncertainty. (d) Principal directions of the distributed moment sources, with compression shown in red and extension shown in blue. Wedges provide the two standard deviation range of the larger strain rate direction. (e–f) Observed and predicted strike-slip rates along the Yushu-Xianshuihe-Xiaojiang fault (e) and the Kunlun fault (f). Geologic estimates are shown as red dots with error bars. Blue and green dots represent classic and deformable block models, respectively. Orange dots denote results from the direct inversion of strain rates.

preferred model, moment rates are almost evenly distributed on the mapped faults and away from the faults. It is worth noting that almost half of the total seismic moment has been released in areas where the strain rates are 25 nanostrain/year or lower, with around 10% released in regions where the strain rates do not exceed 10 nanostrain/year (Figure S23 in Supporting Information S1). This emphasizes the importance of considering seismic hazard in low-interseismic-strain regions, such as those where the 2008 $M_W$ 7.9 Wenchuan earthquake and the 2021 $M_W$ 7.4 Maduo earthquake occurred (e.g., Fang et al., 2022). Despite a slight under-prediction of dilatation away from the main mapped faults (Figure 2), we suggest that the substantial distributed moment sources are necessary to account for the observed diffuse strain. Extensional moment sources are prevalent on the plateau regions while compressional sources dominate in the surrounding areas (Figure 3d); this pattern aligns well with geological and seismological observations (Molnar & Deng, 1984; Molnar & Tapponnier, 1978). The distributed moment sources are likely some combination of elastic strain due to coupling on unmodeled faults and anelastic processes associated strain, such as folding, pressure solution creep (e.g., He et al., 2018), and other relevant mechanisms.

## 6. Conclusions

We have derived high-resolution (∼l km) maps of velocities and strain rates covering 1.3 million km$^2$ across the southeastern Tibetan Plateau. Utilizing these maps, we performed inversions to estimate slip (deficit) rates on recently updated faults using different geodetic deformation modeling approaches. The incorporation of high-resolution InSAR data sharpens the identification of focused shear strain on the major faults and confirms the absence of significant strain concentrations away from faults (whilst still imaging distributed off-fault strain). While the three geodetic deformation models developed in this study generally yield fault slip rates broadly consistent with geological estimates, small systematic differences exist. The geodetically-derived slip rates tend to fall on the low end of the geologic rates for faults that slip lower than ∼5 mm/yr, but exhibit a trend toward the high end for faster-slipping faults (>∼5 mm/yr). Notably, block models tend to overpredict strain on bounding structures and toward fault tips, while underpredicting distributed strain within block interiors. Direct inversion of strain rates reveals that the total deformation is approximately equally balanced between strain localization on the main mapped faults and distributed deformation. As high-resolution strain rate fields become more accessible, we advocate for prioritizing direct inversion over conventional block modeling methods.

## Data Availability Statement

All interferograms are freely downloadable through the COMET-LiCSAR portal (https://comet.nerc.ac.uk/comet-lics-portal/). The derived LOS velocities and their associated uncertainties, as well as the strain rate fields, are available in Fang, Wright, et al. (2024). The GNSS velocities used in this study are compiled from the literature (Fang, Houseman, et al., 2024, and references therein) and archived in Rollins (2023). The *SlideFS* code used to invert strain rates for slip deficit rates is publicly available in Johnson (2024).

## References

Avouac, J.-P., & Tapponnier, P. (1993). Kinematic model of active deformation in Central Asia. *Geophysical Research Letters*, *20*(10), 895–898. https://doi.org/10.1029/93GL00128

Bird, P. (2009). Long-term fault slip rates, distributed deformation rates, and forecast of seismicity in the western United States from joint fitting of community geologic, geodetic, and stress direction data sets. *Journal of Geophysical Research*, *114*(B11). https://doi.org/10.1029/2009JB006317

Chen, Q., Freymueller, J. T., Wang, Q., Yang, Z., Xu, C., & Liu, J. (2004). A deforming block model for the present-day tectonics of Tibet. *Journal of Geophysical Research*, *109*(B1). https://doi.org/10.1029/2002JB002151

Chuang, R. Y., & Johnson, K. M. (2011). Reconciling geologic and geodetic model fault slip-rate discrepancies in Southern California: Consideration of nonsteady mantle flow and lower crustal fault creep. *Geology*, *39*(7), 627–630. https://doi.org/10.1130/G32120.1

DeVries, P. M., Krastev, P. G., Dolan, J. F., & Meade, B. J. (2017). Viscoelastic block models of the North Anatolian fault: A unified earthquake cycle representation of pre-and postseismic geodetic observations. *Bulletin of the Seismological Society of America*, *107*(1), 403–417. https://doi.org/10.1785/0120160059

Dziewonski, A. M., Chou, T. A., & Woodhouse, J. H. (1981). Determination of earthquake source parameters from waveform data for studies of global and regional seismicity. *Journal of Geophysical Research*, *86*(B4), 2825–2852. https://doi.org/10.1029/JB086iB04p02825

Ekström, G., Nettles, M., & Dziewoński, A. (2012). The global CMT project 2004–2010: Centroid-moment tensors for 13,017 earthquakes. *Physics of the Earth and Planetary Interiors*, *200*, 1–9. https://doi.org/10.1016/j.pepi.2012.04.002

Elston, H., Cooke, M., Loveless, J., & Marshall, S. (2024). A new method to invert for interseismic deep slip along closely spaced faults using surface velocities and subsurface stressing-rate tensors. *Earth and Space Science*, *11*(1), e2023EA003069. https://doi.org/10.1029/2023EA003069

Engwirda, D. (2014). Locally optimal delaunay-refinement and optimisation-based mesh generation (Thesis).

Evans, E. L. (2022). A dense block model representing western continental United States deformation for the 2023 update to the national seismic hazard model. *Seismological Research Letters*, *93*(6), 3024–3036. https://doi.org/10.1785/0220220141

Fang, J., Houseman, G., Wright, T., Evans, L., Craig, T., Elliott, J., & Hooper, A. (2024). The dynamics of the India-Eurasia collision: Faulted viscous continuum models constrained by high-resolution sentinel-1 InSAR and GNSS velocities. *Journal of Geophysical Research: Solid Earth*, *129*(6). https://doi.org/10.1029/2023JB028571

Fang, J., Ou, Q., Wright, T. J., Okuwaki, R., Amey, R. M., Craig, T. J., et al. (2022). Earthquake cycle deformation associated with the 2021 MW 7.4 Maduo (Eastern Tibet) earthquake: An intrablock rupture event on a slow-slipping fault from Sentinel-1 InSAR and teleseismic data. *Journal of Geophysical Research: Solid Earth*, *127*(11), e2022JB024268. https://doi.org/10.1029/2022JB024268

Fang, J., Wright, T. J., Johnson, K. M., Ou, Q., Styron, R., Craig, T. J., et al. (2024). Strain partitioning in the southeastern Tibetan Plateau from kinematic modeling of high-resolution sentinel-1 InSAR and GNSS [Dataset]. *Zenodo*. https://doi.org/10.5281/zenodo.13731812

Fialko, Y. (2021). Estimation of absolute stress in the hypocentral region of the 2019 ridgecrest, California, earthquakes. *Journal of Geophysical Research: Solid Earth*, *126*(7), e2021JB022000. https://doi.org/10.1029/2021JB022000

Gordon, R. G. (2023). Tectonic strain rates, diffuse oceanic plate boundaries, and the plate tectonic approximation. In *Dynamics of plate tectonics and mantle convection* (pp. 83–103). Elsevier. https://doi.org/10.1016/B978-0-323-85733-8.00024-X

Hammond, W. C., Kreemer, C., & Blewitt, G. (2024). Robust imaging of fault slip rates in the Walker Lane and western Great Basin from GPS data using a multi-block model approach. *Journal of Geophysical Research: Solid Earth*, *129*(3), e2023JB028044. https://doi.org/10.1029/2023JB028044

Hatem, A. E., Reitman, N. G., Briggs, R. W., Gold, R. D., Thompson Jobe, J. A., & Burgette, R. J. (2022). Western U.S. Geologic deformation model for use in the U.S. National seismic hazard model 2023. *Seismological Research Letters*, *93*(6), 3053–3067. https://doi.org/10.1785/0220220154

He, X., Li, H., Wang, H., Zhang, L., Xu, Z., & Si, J. (2018). Creeping along the guanxian-anxian fault of the 2008 Mw 7.9 wenchuan earthquake in the longmen Shan, China. *Tectonics*, *37*(7), 2124–2141. https://doi.org/10.1029/2017TC004820

Hetland, E. A., & Hager, B. H. (2005). Postseismic and interseismic displacements near a strike-slip fault: A two-dimensional theory for general linear viscoelastic rheologies. *Journal of Geophysical Research*, *110*(B10). https://doi.org/10.1029/2005JB003689

Hussain, E., Wright, T. J., Walters, R. J., Bekaert, D. P., Lloyd, R., & Hooper, A. (2018). Constant strain accumulation rate between major earthquakes on the North Anatolian Fault. *Nature Communications*, *9*(1), 1–9. https://doi.org/10.1038/s41467-018-03739-2

Johnson, K. M. (2024). SliDeFS v2.0.0 [Software]. *Zenodo*. https://doi.org/10.5281/zenodo.12583880

Johnson, K. M., & Fukuda, J. (2010). New methods for estimating the spatial distribution of locked asperities and stress-driven interseismic creep on faults with application to the San Francisco Bay Area, California. *Journal of Geophysical Research*, *115*(B12). https://doi.org/10.1029/2010JB007703

Johnson, K. M., Wallace, L. M., Maurer, J., Hamling, I., Williams, C., Rollins, C., et al. (2024). Inverting geodetic strain rates for slip deficit rate in complex deforming zones: An application to the New Zealand plate boundary. *Journal of Geophysical Research: Solid Earth*, *129*(3), e2023JB027565. https://doi.org/10.1029/2023JB027565

Lambert, V., & Barbot, S. (2016). Contribution of viscoelastic flow in earthquake cycles within the lithosphere-asthenosphere system. *Geophysical Research Letters*, *43*(19), 10–142. https://doi.org/10.1002/2016GL070345

Lazecky, M., Spaans, K., González, P. J., Maghsoudi, Y., Morishita, Y., Albino, F., et al. (2020). LiCSAR: An automatic InSAR tool for measuring and monitoring tectonic and volcanic activity. *Remote Sensing*, *12*(15), 2430. https://doi.org/10.3390/rs12152430

Li, Y., & Bürgmann, R. (2021). Partial coupling and earthquake potential along the Xianshuihe Fault, China. *Journal of Geophysical Research: Solid Earth*, *126*(7), e2020JB021406. https://doi.org/10.1029/2020JB021406

Li, Y., Liu, M., Li, Y., & Chen, L. (2019). Active crustal deformation in southeastern Tibetan Plateau: The kinematics and dynamics. *Earth and Planetary Science Letters*, *523*, 115708. https://doi.org/10.1016/j.epsl.2019.07.010

Li, Y., Shan, X., Gao, Z., & Huang, X. (2023). Interseismic coupling, asperity distribution, and earthquake potential on major faults in southeastern Tibet. *Geophysical Research Letters*, *50*(8), e2022GL101209. https://doi.org/10.1029/2022GL101209

Li, Y., Song, S., Hao, M., Zhuang, W., Cui, D., Yang, F., & Wang, Q. (2023). Present–day crustal deformation across the Daliang Shan, southeastern Tibetan Plateau constrained by a dense GPS network. *Geophysical Journal International*, *232*(3), 1619–1638. https://doi.org/10.1093/gji/ggac412

Loveless, J. P., & Meade, B. J. (2011). Partitioning of localized and diffuse deformation in the Tibetan Plateau from joint inversions of geologic and geodetic observations. *Earth and Planetary Science Letters*, *303*(1), 11–24. https://doi.org/10.1016/j.epsl.2010.12.014

McCaffrey, R. (2009). Time-dependent inversion of three-component continuous GPS for steady and transient sources in northern Cascadia. *Geophysical Research Letters*, *36*(7). https://doi.org/10.1029/2008GL036784

McKenzie, D. (1972). Active tectonics of the mediterranean region. *Geophysical Journal International*, *30*(2), 109–185. https://doi.org/10.1111/j.1365-246X.1972.tb02351.x

Meade, B. J. (2007). Present-day kinematics at the India-Asia collision zone. *Geology*, *35*(1), 81–84. https://doi.org/10.1130/g22924a.1

Meade, B. J., & Hager, B. H. (2005). Block models of crustal motion in southern California constrained by GPS measurements. *Journal of Geophysical Research*, *110*(B3). https://doi.org/10.1029/2004JB003209

Meade, B. J., & Loveless, J. P. (2009). Block modeling with connected fault-network geometries and a linear elastic coupling estimator in spherical coordinates. *Bulletin of the Seismological Society of America*, *99*(6), 3124–3139. https://doi.org/10.1785/0120090088

Molnar, P., & Deng, Q. (1984). Faulting associated with large earthquakes and the average rate of deformation in central and eastern Asia. *Journal of Geophysical Research*, *89*(B7), 6203–6227. https://doi.org/10.1029/JB089iB07p06203

Molnar, P., & Tapponnier, P. (1978). Active tectonics of Tibet. *Journal of Geophysical Research*, *83*(B11), 5361–5375. https://doi.org/10.1029/JB083iB11p05361

Morishita, Y., Lazecky, M., Wright, T. J., Weiss, J. R., Elliott, J. R., & Hooper, A. (2020). LiCSBAS: An open-source InSAR time series analysis package integrated with the LiCSAR automated sentinel-1 InSAR processor. *Remote Sensing*, *12*(3), 424. https://doi.org/10.3390/rs12030424

Otofuji, Y.-i., Yokoyama, M., Kitada, K., & Zaman, H. (2010). Paleomagnetic versus GPS determined tectonic rotation around eastern Himalayan syntaxis in East Asia. *Journal of Asian Earth Sciences*, *37*(5–6), 438–451. https://doi.org/10.1016/j.jseaes.2009.11.003

Ou, Q., Daout, S., Weiss, J. R., Shen, L., Lazecký, M., Wright, T. J., & Parsons, B. E. (2022). Large-scale interseismic strain mapping of the NE Tibetan Plateau from sentinel-1 interferometry. *Journal of Geophysical Research: Solid Earth*, *127*(6), e2022JB024176. https://doi.org/10.1029/2022JB024176

Pang, Y., Wu, Y., Li, Y., & Chen, C. (2023). The mechanism of the present-day crustal deformation in southeast Tibet: From numerical modelling and geodetic observations. *Geophysical Journal International*, *235*(1), 12–23. https://doi.org/10.1093/gji/ggad200

Pollitz, F. F. (2022). Viscoelastic Fault-based model of crustal deformation for the 2023 update to the U.S. National seismic hazard model. *Seismological Research Letters*, *93*(6), 3087–3099. https://doi.org/10.1785/0220220137

Pollitz, F. F., & Evans, E. L. (2017). Implications of the earthquake cycle for inferring fault locking on the Cascadia megathrust. *Geophysical Journal International*, *209*(1), 167–185. https://doi.org/10.1093/gji/ggx009

Pollitz, F. F., McCrory, P., Wilson, D., Svarc, J., Puskas, C., & Smith, R. B. (2010). Viscoelastic-cycle model of interseismic deformation in the northwestern United States. *Geophysical Journal International*, *181*(2), 665–696. https://doi.org/10.1111/j.1365-246X.2010.04546.x

Qiao, X., & Zhou, Y. (2021). Geodetic imaging of shallow creep along the Xianshuihe fault and its frictional properties. *Earth and Planetary Science Letters*, *567*, 117001. https://doi.org/10.1016/j.epsl.2021.117001

Rollins, C. (2023). earjcr1/AHB_GPS: v0.1 (v0.1) [Dataset]. *Zenodo*. https://doi.org/10.5281/zenodo.10372924

Savage, J. C., & Burford, R. (1973). Geodetic determination of relative plate motion in central California. *Journal of Geophysical Research*, *78*(5), 832–845. https://doi.org/10.1029/JB078i005p00832

Shan, B., Xiong, X., Zheng, Y., & Diao, F. (2009). Stress changes on major faults caused by Mw7.9 Wenchuan earthquake, May 12, 2008. *Science in China - Series D: Earth Sciences*, *52*(5), 593–601. https://doi.org/10.1007/s11430-009-0060-9

Shen, Z.-K., & Bird, P. (2022). NeoKinema deformation model for the 2023 update to the U.S. National seismic hazard model. *Seismological Research Letters*, *93*(6), 3037–3052. https://doi.org/10.1785/0220220179

Shen, Z.-K., Lü, J., Wang, M., & Bürgmann, R. (2005). Contemporary crustal deformation around the southeast borderland of the Tibetan Plateau. *Journal of Geophysical Research*, *110*(B11). https://doi.org/10.1029/2004JB003421

Shen, Z.-K., Wang, M., Zeng, Y., & Wang, F. (2015). Optimal interpolation of spatially discretized geodetic data. *Bulletin of the Seismological Society of America*, *105*(4), 2117–2127. https://doi.org/10.1785/0120140247

Styron, R. (2022). Contemporary slip rates of all active faults in the indo-Asian collision zone. *ESS Open Archive*. https://doi.org/10.1002/essoar.10512747.1

Thatcher, W. (2007). Microplate model for the present-day deformation of Tibet. *Journal of Geophysical Research*, *112*(B1). https://doi.org/10.1029/2005JB004244

Tong, Y., Yang, Z., Pei, J., Wang, H., Wu, Z., & Li, J. (2021). Crustal clockwise rotation of the southeastern edge of the Tibetan Plateau since the late Oligocene. *Journal of Geophysical Research: Solid Earth*, *126*(1), e2020JB020153. https://doi.org/10.1029/2020JB020153

Van Dissen, R. J., Johnson, K. M., Seebeck, H., Wallace, L. M., Rollins, C., Maurer, J., et al. (2023). Upper Plate and subduction interface deformation models in the 2022 revision of the Aotearoa New Zealand national seismic hazard model. *Bulletin of the Seismological Society of America*, *114*(1), 37–56. https://doi.org/10.1785/0120230118

Wang, H., & Wright, T. J. (2012). Satellite geodetic imaging reveals internal deformation of western Tibet. *Geophysical Research Letters*, *39*(7). https://doi.org/10.1029/2012GL051222

Wang, M., & Shen, Z.-K. (2020). Present-Day crustal deformation of continental China derived from GPS and its tectonic implications. *Journal of Geophysical Research: Solid Earth*, *125*(2), e2019JB018774. https://doi.org/10.1029/2019JB018774

Wang, M., Shen, Z.-K., Wang, Y.-Z., Bürgmann, R., Wang, F., Zhang, P.-Z., et al. (2021). Postseismic deformation of the 2008 wenchuan earthquake illuminates lithospheric rheological structure and dynamics of Eastern Tibet. *Journal of Geophysical Research: Solid Earth*, *126*(9), e2021JB022399. https://doi.org/10.1029/2021JB022399

Wang, W., Qiao, X., & Ding, K. (2021). Present-day kinematics in southeastern Tibet inferred from GPS measurements. *Journal of Geophysical Research: Solid Earth*, *126*(1), e2020JB021305. https://doi.org/10.1029/2020JB021305

Wang, W., Qiao, X., Yang, S., & Wang, D. (2017). Present-day velocity field and block kinematics of Tibetan Plateau from GPS measurements. *Geophysical Journal International*, *208*(2), 1088–1102. https://doi.org/10.1093/gji/ggw445

Weiss, J. R., Walters, R. J., Morishita, Y., Wright, T. J., Lazecky, M., Wang, H., et al. (2020). High-resolution surface velocities and strain for anatolia from sentinel-1 InSAR and GNSS data. *Geophysical Research Letters*, *47*(17), e2020GL087376. https://doi.org/10.1029/2020GL087376

Wessel, P., Smith, W. H. F., Scharroo, R., Luis, J., & Wobbe, F. (2013). Generic mapping tools: Improved version released. *Eos, Transactions American Geophysical Union*, *94*(45), 409–410. https://doi.org/10.1002/2013EO450001

Wright, T. J., Parsons, B. E., & Lu, Z. (2004). Toward mapping surface deformation in three dimensions using InSAR. *Geophysical Research Letters*, *31*(1). https://doi.org/10.1029/2003GL018827

Xu, X. (2022). *China active fault database*. Active Fault Survey Data Centre at Institute of Geology, China Earthquake Administration. https://doi.org/10.12031/activefault.china.400.2022.db

Zeng, Y. (2022). A fault-based crustal deformation model with deep driven dislocation sources for the 2023 update to the U.S. National seismic hazard model. *Seismological Research Letters*, *93*(6), 3170–3185. https://doi.org/10.1785/0220220209

Zeng, Y., & Shen, Z. (2017). A fault-based model for crustal deformation in the western United States based on a combined inversion of GPS and geologic inputs. *Bulletin of the Seismological Society of America*, *107*(6), 2597–2612. https://doi.org/10.1785/0120150362

Zeng, Y., & Shen, Z.-K. (2014). Fault network modeling of crustal deformation in California constrained using GPS and geologic observations. *Tectonophysics*, *612–613*, 1–17. https://doi.org/10.1016/j.tecto.2013.11.030

Zhao, D., Qu, C., Shan, X., Gong, W., Weng, H., Chen, H., & Wu, D. (2024). An updated fault coupling model along major block-bounding faults on the eastern and northeastern Tibetan plateau from a stress-constrained inversion of GPS and InSAR data. *Journal of Geophysical Research: Solid Earth*, *129*(4), e2023JB028483. https://doi.org/10.1029/2023JB028483

Zhao, G., Meng, G., Wu, W., Su, X., & Pan, Z. (2022). Earthquake potential assessment around the southeastern Tibetan plateau based on seismic and geodetic data. *Pure and Applied Geophysics*, *179*(1), 11–44. https://doi.org/10.1007/s00024-021-02917-6

Zheng, G., Wang, H., Wright, T. J., Lou, Y., Zhang, R., Zhang, W., et al. (2017). Crustal deformation in the India-Eurasia collision zone from 25 Years of GPS measurements. *Journal of Geophysical Research: Solid Earth*, *122*(11), 9290–9312. https://doi.org/10.1002/2017JB014465

Zhu, S., Chen, C., Zhan, W., Li, J., Guo, N., Li, X., & Su, G. (2023). Joint adjustment of strain rate fields and its application in shallow seismicity forecast in the Sichuan-Yunnan region, China. *Acta Geodaetica et Geophysica*, *58*(4), 499–513. https://doi.org/10.1007/s40328-023-00424-9

## References From the Supporting Information

Aki, K., & Richards, P. G. (1980). *Quantitative seismology*. W.H. Freeman and Company.

Ansari, H., Zan, F. D., & Parizzi, A. (2021). Study of systematic bias in measuring surface deformation with SAR interferometry. *IEEE Transactions on Geoscience and Remote Sensing*, *59*(2), 1285–1301. https://doi.org/10.1109/TGRS.2020.3003421

Chen, C. W., & Zebker, H. A. (2000). Network approaches to two-dimensional phase unwrapping: Intractability and two new algorithms. *Journal of the Optical Society of America A*, *17*(3), 401–414. https://doi.org/10.1364/JOSAA.17.000401

Chen, C. W., & Zebker, H. A. (2001). Two-dimensional phase unwrapping with use of statistical models for cost functions in nonlinear optimization. *Journal of the Optical Society of America A*, *18*(2), 338–351. https://doi.org/10.1364/JOSAA.18.000338

Chen, C. W., & Zebker, H. A. (2002). Phase unwrapping for large SAR interferograms: Statistical segmentation and generalized network models. *IEEE Transactions on Geoscience and Remote Sensing*, *40*(8), 1709–1719. https://doi.org/10.1109/TGRS.2002.802453

Fukahata, Y., & Wright, T. J. (2008). A non-linear geodetic data inversion using ABIC for slip distribution on a fault with an unknown dip angle. *Geophysical Journal International*, *173*(2), 353–364. https://doi.org/10.1111/j.1365-246X.2007.03713.x

Fukuda, J., & Johnson, K. M. (2008). A fully Bayesian inversion for spatial distribution of fault slip with objective smoothing. *Bulletin of the Seismological Society of America*, *98*(3), 1128–1146. https://doi.org/10.1785/0120070194

Herman, M. W., & Govers, R. (2020). Locating fully locked asperities along the south America subduction megathrust: A new physical interseismic inversion approach in a Bayesian framework. *Geochemistry, Geophysics, Geosystems*, *21*(8), e2020GC009063. https://doi.org/10.1029/2020GC009063

Huang, Z., Zhou, Y., Qiao, X., Zhang, P., & Cheng, X. (2022). Kinematics of the 1000 km Haiyuan fault system in Northeastern Tibet from high-resolution Sentinel-1 InSAR velocities: Fault architecture, slip rates, and partitioning. *Earth and Planetary Science Letters*, *583*, 117450. https://doi.org/10.1016/j.epsl.2022.117450

Jiang, Y., Samsonov, S. V., & González, P. J. (2022). Aseismic Fault slip during a shallow normal-faulting seismic swarm constrained using a physically informed geodetic inversion method. *Journal of Geophysical Research: Solid Earth*, *127*(7), e2021JB022621. https://doi.org/10.1029/2021JB022621

Kreemer, C., Blewitt, G., & Klein, E. C. (2014). A geodetic plate motion and global strain rate model. *Geochemistry, Geophysics, Geosystems*, *15*(10), 3849–3889. https://doi.org/10.1002/2014GC005407

Maghsoudi, Y., Hooper, A. J., Wright, T. J., Lazecky, M., & Ansari, H. (2022). Characterizing and correcting phase biases in short-term, multilooked interferograms. *Remote Sensing of Environment*, *275*, 113022. https://doi.org/10.1016/j.rse.2022.113022

Matthews, M. V., & Segall, P. (1993). Estimation of depth-dependent fault slip from measured surface deformation with application to the 1906 San Francisco Earthquake. *Journal of Geophysical Research*, *98*(B7), 12153–12163. https://doi.org/10.1029/93JB00440

Minson, S. E., Simons, M., & Beck, J. L. (2013). Bayesian inversion for finite fault earthquake source models I—Theory and algorithm. *Geophysical Journal International*, *194*(3), 1701–1726. https://doi.org/10.1093/gji/ggt180

Mosegaard, K., & Tarantola, A. (1995). Monte Carlo sampling of solutions to inverse problems. *Journal of Geophysical Research*, *100*(B7), 12431–12447. https://doi.org/10.1029/94JB03097

Ou, Q., Elliott, J. R., Maghsoudi, Y., Rollins, C., Lazecky, M., & Wright, T. J. (2023). Tectonic, climatic and anthropogenic deformation over the Tianshan mountains. *AGU Fall Meeting Abstracts* (Vol. 2023, pp. G11A-05).

Qiao, X., Zhou, Y., & Zhang, P. (2022). Along-strike variation in fault structural maturity and seismic moment deficits on the Yushu-Ganzi-Xianshuihe fault system revealed by strain accumulation and regional seismicity. *Earth and Planetary Science Letters*, *596*, 117799. https://doi.org/10.1016/j.epsl.2022.117799

Sandwell, D. T., & Wessel, P. (2016). Interpolation of 2-D vector data using constraints from elasticity. *Geophysical Research Letters*, *43*(20), 10–703. https://doi.org/10.1002/2016GL070340

Segall, P. (2010). *Earthquake and volcano deformation*. Princeton University Press.

Yu, C., Li, Z., Penna, N. T., & Crippa, P. (2018). Generic atmospheric correction model for interferometric synthetic aperture radar observations. *Journal of Geophysical Research: Solid Earth*, *123*(10), 9202–9222. https://doi.org/10.1029/2017JB015305